Compressive behaviour of alkali-activated slag-based concrete and Portland cement concrete incorporating novel multiple hooked-end steel fibres

Laura Rossi · **Ravi A. Patel** · **Frank Dehn**

Abstract This study investigates the effect of single and multiple hooked-end steel fibres on the mechanical properties of alkali-activated slag-based concrete (AASC) and compares its performance with a similar strength-grade Portland cement concrete (PCC). Three different fibre geometries, i.e. single (Dramix® 3D), double (Dramix® 4D) and triple hooked-end (Dramix® 5D) steel fibres, and three different volume fractions, i.e. 0.25%, 0.50% and 0.75% are considered. Compressive strength, modulus of elasticity and stress–strain response under uniaxial compression are evaluated. Hooked-end steel fibres have a limited effect on the compressive strength and modulus of elasticity of both AASC and PCC, regardless of fibre geometry and content. Although hooked-end steel fibres improve the compressive stress–strain behaviour of both composites, higher enhancement of peak stress, corresponding strain and post-peak response is observed for fibre-reinforced AASC (FRAASC) mixtures. To predict the stress–strain response under uniaxial compression of steel FRAASC a new analytical model is proposed and calibrated using an extensive dataset of experimental stress–strain curves available in the literature for both steel fibre-reinforced PCC and AASC. This model can predict the compressive stress–strain behaviour of FRAASC using the compressive peak stress and corresponding strain of the unreinforced matrix and the steel fibre reinforcing index (RI_v) as inputs and provides excellent results when validated against the data obtained in this study for FRAASC.

L. Rossi (✉) · R. A. Patel · F. Dehn
Institute of Building Materials and Concrete Structures (IMB), Karlsruhe Institute of Technology (KIT), 76131 Karlsruhe, Germany
e-mail: laura.rossi@kit.edu

R. A. Patel
e-mail: ravi.patel@kit.edu

F. Dehn
e-mail: frank.dehn@kit.edu

L. Rossi · R. A. Patel · F. Dehn
Material Testing and Research Institute Karlsruhe (MPA), Karlsruhe Institute of Technology (KIT), 76131 Karlsruhe, Germany

1 Introduction

Alkali-activated slag concrete (AASC) has been the subject of in-depth research in recent years as a more environmentally friendly alternative to Portland cement (PC) as a binder for concrete [1–7]. Alkali-

activated slag concrete exhibits comparable or even better mechanical and durability performance than traditional PC concrete (PCC), such as higher early-age strength and higher stability in aggressive environments [1, 4, 7–13]. Despite its promising nature, AASC exhibits more brittle behaviour than cement-based concrete [14, 15], which can be attributed to the higher autogenous shrinkage-induced micro-cracking of AASC [1, 6, 11, 12, 15–18]. This restricts the applicability of AASC in areas requiring high flexural and tensile capacity. Several studies [9, 11–13, 18–21] demonstrated that the addition of randomly distributed steel fibres is an effective way to overcome the brittleness of the alkali-activated slag-based matrix. Transferring stresses across the cracked surfaces and increasing the energy needed for crack growth, fibres mitigate crack formation and propagation. The crack bridging capacity of the fibres enhances the ductility, fracture toughness and post-cracking load-bearing capacity of the composite [11, 18]. The efficiency of fibre bridging ability largely depends on the fibre-matrix interface bond [20, 22–24]. Thus, novel multiple hooked-end fibres have been developed to improve the fibre's mechanical anchorage, tensile strength and ductility. Unlike the old generation of single hooked-end steel fibres, generally known as 3D fibres, novel multiple hooked-end steel fibres are characterised by improved geometry, i.e., additional bends at both ends of the fibre, resulting in double (4D) and triple (5D) hooked-end steel fibres. Several studies investigated the pull-out behaviour [24–26] and the influence of novel hooked-end steel fibre geometry on the post-cracking behaviour of cementitious composites [23, 27–30]. Lee et al. [27] and Abdallah et al. [29] demonstrated that the incorporation of 3D, 4D and 5D fibres up to a volume fraction of 1% has a limited effect on the compressive strength. However, fibre geometry and volume fraction significantly affect the flexural behaviour of the composite, with 4D and 5D fibres showing higher flexural strength than 3D fibres. Although several studies investigate the effect of the addition of multiple hooked-end steel fibres on the mechanical properties of cementitious composites, very few investigations focus on the incorporation of these fibres in alkali-activated slag-based concrete. Shaikh [20] investigated only the pull-out behaviour of 3D, 4D and 5D fibres in alkali-activated fly ash-based and alkali-activated fly ash-slag mortars. El-Hassan and Elkholy [6] evaluated the effect of hybrid steel fibre reinforcement in blended alkali-activated concrete, i.e. different proportions of 3D, 4D and 5D fibres were added in an alkali-activated slag-fly ash matrix. However, the effect of each fibre geometry on the performance of alkali-activated slag-based concrete has not been evaluated. The understanding of the effect of novel hooked-end steel fibres on the compressive and tensile stress–strain behaviour of alkali-activated slag concrete is still lacking. Evaluating the full-range stress–strain response of the composite under both compression and tension is fundamental to fully characterise newly developed construction materials such as fibre-reinforced AASC (FRAASC) and derive constitutive models for design and field applications.

Different analytical models have been developed to predict the behaviour of steel fibre-reinforced Portland cement concrete (FRPCC) under uniaxial compression [31–35]. The majority of these models are based on the model proposed by Carreira and Chu [36] for plain concrete and modified by Ezeldin and Balaguru [35] for steel FRPCC. Equation (1) provides the general formula of these previously mentioned models while the available analytical models for steel FRPCC are summarised in Table 1.

$$\frac{\sigma_c}{\sigma_{c,\max(FRC)}} = \frac{\beta\left(\varepsilon_c / \varepsilon_{c,\max(FRC)}\right)}{\beta - 1 + \left(\varepsilon_c / \varepsilon_{c,\max(FRC)}\right)^{\beta}} \qquad (1)$$

where σ_c is the compressive stress, $\sigma_{c,\max(FRC)}$ is the maximum compressive stress (compressive strength), ε_c is the uniaxial strain, $\varepsilon_{c,\max(FRC)}$ is the uniaxial strain corresponding to $\sigma_{c,\max(FRC)}$ and β is a material parameter. Most of the models summarised in Table 1 were fitted on a small set of experimental results, making each model strictly dependent on the test conditions [7] and the characteristics of both the matrix and the steel fibre type investigated. Furthermore, many models provide a single equation to describe the entire compressive stress–strain curve without considering the different effects of fibre geometry and volume fraction on the pre- and post-peak branch of the stress–strain curve. Only Ruiz et al. [37] and Lee et al. [38] developed a model based on two separate equations to describe the stress–strain curve under compression and take into account the different effects of steel fibre incorporation on the material behaviour. Although the equation proposed by Ruiz et al. [37] for $\varepsilon_c < \varepsilon_{c,\max(FRC)}$ can predict quite

Table 1 Analytical models for the compressive behaviour of steel fibre-reinforced PC concrete (PCC) and plain alkali-activated fly ash (AAFA) and fly ash-slag (AAFA/GGBS) concrete

References	Matrix type	Fibre type	Fibre geometry (l_f/d_f)	Fibre content	Analytical model and coefficients
Carreira and Chu [36]	PCC	–	–	–	$\frac{\sigma_c}{\sigma_{c,\max(REF)}} = \frac{\beta\left(\varepsilon_c/\varepsilon_{c,\max(REF)}\right)}{\beta-1+\left(\varepsilon_c/\varepsilon_{c,\max(REF)}\right)^{\beta}}$ $\beta = \frac{1}{1-\left(\frac{\sigma_{c,\max(REF)}}{\varepsilon_{c,\max(REF)}E_{it(REF)}}\right)}$ $\varepsilon_{c,\max(REF)} = (4.88\sigma_{c,\max(REF)} + 168)10^{-5}$
Ezeldin and Balaguru [35]	PCC	HE	50/05 60/0.8 30/0.5	30 kg/m³ 45 kg/m³ 60 kg/m³	$\frac{\sigma_c}{\sigma_{c,\max(FRC)}} = \frac{\beta\left(\varepsilon_c/\varepsilon_{c,\max(FRC)}\right)}{\beta-1+\left(\varepsilon_c/\varepsilon_{c,\max(FRC)}\right)^{\beta}}$ $\beta = 1.093 + 0.7132(RI_w)^{-0.926}$ $\sigma_{c,\max(FRC)} = \sigma_{c,\max(REF)} + 3.51(RI_w)$ $\varepsilon_{c,\max(FRC)} = \varepsilon_{c,\max(REF)} + 446\times10^{-6}(RI_w)$
Nataraja et al. [31]	PCC	C	27.5/0.5 41/0.5	39 kg/m³ 58 kg/m³ 78 kg/m³	$\frac{\sigma_c}{\sigma_{c,\max(FRC)}} = \frac{\beta\left(\varepsilon_c/\varepsilon_{c,\max(FRC)}\right)}{\beta-1+\left(\varepsilon_c/\varepsilon_{c,\max(FRC)}\right)^{\beta}}$ $\beta = 0.5811 + 1.93(RI_w)^{-0.7406}$ $\sigma_{c,\max(FRC)} = \sigma_{c,\max(REF)} + 2.1604(RI_w)$ $\varepsilon_{c,\max(FRC)} = \varepsilon_{c,\max(REF)} + 0.0006(RI_w)$
De Oliveira Junior et al. [32]	PCC	HE	35/0.55	1.00% 2.00%	$\frac{\sigma_c}{\sigma_{c,\max(FRC)}} = \frac{\beta\left(\varepsilon_c/\varepsilon_{c,\max(FRC)}\right)}{\beta-1+\left(\varepsilon_c/\varepsilon_{c,\max(FRC)}\right)^{\beta}}$ $\beta = (0.0536 - 0.574v_f)\sigma_{c,\max(FRC)}$ $\varepsilon_{c,\max(FRC)} = (0.00048 + 0.01886v_f)\ln\sigma_{c,\max(FRC)}$
Ou et al. [33]	PCC	HE	30/0.5 30/0.6 35/0.5 50/0.5 50/1.0 60/1.0	0%–3.40%	$\frac{\sigma_c}{\sigma_{c,\max(FRC)}} = \frac{\beta\left(\varepsilon_c/\varepsilon_{c,\max(FRC)}\right)}{\beta-1+\left(\varepsilon_c/\varepsilon_{c,\max(FRC)}\right)^{\beta}}$ $\beta = 0.71(RI_v)^2 - 2.00RI_v + 3.05$ $\sigma_{c,\max(FRC)} = \sigma_{c,\max(REF)} + 2.35(RI_v)$ $\varepsilon_{c,\max(FRC)} = \varepsilon_{c,\max(REF)} + 0.0007(RI_v)$
Abbas et al. [34]	PCC	HE	40/0.62 50/0.62 60/0.75	0.50% 1.00% 1.50%	$\frac{\sigma_c}{\sigma_{c,\max(FRC)}} = \frac{\beta\left(\varepsilon_c/\varepsilon_{c,\max(FRC)}\right)}{\beta-1+\left(\varepsilon_c/\varepsilon_{c,\max(FRC)}\right)^{\beta}}$ $\beta = 1.401(RI_v)^2 - 1.56RI_v + 2.42$ $\sigma_{c,\max(FRC)} = \sigma_{c,\max(REF)} + 5.59(RI_v)$ $\varepsilon_{c,\max(FRC)} = \varepsilon_{c,\max(REF)} + 0.000261(RI_v)$
Lee et al. [38]	PCC	HE	50/1.05 35/0.55 30/0.38	0.50% 1.00% 1.50% 2.00%	$\sigma_c = \sigma_{c,\max(FRC)}\frac{A\left(\varepsilon_c/\varepsilon_{c,\max(FRC)}\right)}{A-1+\left(\varepsilon_c/\varepsilon_{c,\max(FRC)}\right)^{B}}$ $A = B = \frac{1}{1-\left(\frac{\sigma_{c,\max(FRC)}}{\varepsilon_{c,\max(FRC)}E_{c(FRC)}}\right)}, \ \varepsilon/\varepsilon_{c,\max(FRC)} \leq 1$ $\begin{cases} A = 1 + 0.723(RI_v)^{-0.957} \\ B = \left(\frac{\sigma_{c,\max(FRC)}}{50}\right)^{0.064}\left[1 + 0.882(RI_v)^{-0.882}\right] \end{cases}, \ \varepsilon/\varepsilon_{c,\max(FRC)} > 1$ $\varepsilon_{c,\max(FRC)} = (0.0003(RI_v) + 0.0018)\sigma_{c,\max(FRC)}^{0.12}$

Table 1 continued

References	Matrix type	Fibre type	Fibre geometry (l_f/d_f)	Fibre content	Analytical model and coefficients
Ruiz et al. [37,44]	PCC				$\frac{\sigma_c}{\sigma_{c,max(FRC)}} = \begin{cases} \frac{\alpha(\varepsilon_c/\varepsilon_{c,max(FRC)}) - (\varepsilon_c/\varepsilon_{c,max(FRC)})^2}{1 + (\alpha-2)(\varepsilon_c/\varepsilon_{c,max(FRC)})}, & \varepsilon_c/\varepsilon_{c,max(FRC)} \leq 1 \\ 1 - \frac{1}{4}(1-\sigma_R^*)(\varepsilon_c/\varepsilon_{c,max(FRC)} - 1)^2, & \varepsilon_c/\varepsilon_{c,max(FRC)} > 1 \end{cases}$ $\alpha = 1{,}05\ \varepsilon_{c,max(FRC)} \frac{E_{c(FRC)}}{\sigma_{c,max(FRC)}}$ $\sigma_R^* = 0.8279 + 0.3888\ l_f^*(35.03\ v_f - 1),\ l_f^* = l_f/30$ $\sigma_{c,max(FRC)} = \sigma_{c,max(REF)}(1 + 4.17 l_f^* v_f)$ $\varepsilon_{c,max(FRC)} = \varepsilon_{c,max(REF)}[1 + 0.4823\lambda(v_f - 0.002606 l_f^*)]$ λ = fibre aspect ratio
Hardjito et al. [39]	AAFA	–	–	–	$\sigma_c = \sigma_{c,max(REF)} \frac{n(\varepsilon_c/\varepsilon_{c,max(REF)})}{n - 1 + (\varepsilon_c/\varepsilon_{c,max(REF)})^{nk}}$ $n = 0.8 + \left(\frac{\sigma_{c,max(REF)}}{17}\right)$ $k = \begin{cases} 1, & \varepsilon_c/\varepsilon_{c,max(REF)} \leq 1 \\ 0.67 + \left(\frac{\sigma_{c,max(REF)}}{62}\right), & \varepsilon_c/\varepsilon_{c,max(REF)} > 1 \end{cases}$
Noushini et al. [41]	AAFA	–	–	–	$\frac{\sigma_c}{\sigma_{c,max(REF)}} = \frac{n(\varepsilon_c/\varepsilon_{c,max(REF)})}{n - 1 + (\varepsilon_c/\varepsilon_{c,max(REF)})^n}$ $n = \begin{cases} n_1 = [1.02 - 1.17(E_{sec(REF)}/E_{c(REF)})]^{-0.45}, & \varepsilon_c/\varepsilon_{c,max(REF)} \leq 1 \\ n_2 = n_1 + (\omega + 28\zeta), & \varepsilon_c/\varepsilon_{c,max(REF)} > 1 \end{cases}$ $\omega = C(12.4 - 0.015\sigma_{c,max(REF)})^{-0.5}$ $\zeta = 0.83 e^{(-911/\sigma_{c,max(REF)})}$
Cong et al. [42]	AAFA/ GGBS	–	–	–	$\frac{\sigma_c}{\sigma_{c,max(REF)}} = \frac{m(\varepsilon_c/\varepsilon_{c,max(REF)})}{m - 1 + (\varepsilon_c/\varepsilon_{c,max(REF)})^\beta}$ $m = 2.0 + \left(\frac{E_{c(REF)}}{19.5}\right)$ $\beta = 5 + 10\left(\frac{-8.4}{\sigma_{c,max(REF)}}\right)$

HE = hooked-end steel fibres, C = crimped steel fibres, $E_{it(FRC)}$ and $E_{it(REF)}$ = initial secant modulus at 40% of the peak stress for fibre-reinforced and plain concrete, respectively; $E_{c(FRC)}$ and $E_{c(REF)}$ = modulus of elasticity for fibre-reinforced and plain concrete, respectively; l_f = fibre length; v_f = fibre volume fraction; RI_w and RI_v = reinforcing index ($l_f/d_f \bullet v_f$) calculated using the fibre weight and volume fraction, respectively; $\sigma_{c,max(FRC)}$ and $\sigma_{c,max(REF)}$ = compressive strength of fibre-reinforced and plain concrete, respectively; $\varepsilon_{c,max(FRC)}$ and $\varepsilon_{c,max(REF)}$ = strain corresponding to peak stress of fibre-reinforced and plain concrete, respectively

accurately the pre-peak ascending branch of the stress–strain curve of steel FRPCC, the parabolic equation describing the post-peak descending branch is not able to represent the real compressive response of the composite, characterised by exponential softening behaviour. Lee et al. [38] proposed a two-equation model governed by two material parameters. In the pre-peak phase of the stress–strain response under uniaxial compression, the two parameters have the same value and the model corresponds to the one proposed by Ezeldin and Balaguru [35]. In the post-peak phase, the model parameters have different values linked to the fibre reinforcing index RI_v (defined as the product of the fibre aspect ratio (l_f/d_f) and the fibre volume fraction (v_f)) to take into account the fibre-bridging effect once cracks start growing and propagating.

Analytical equations to predict the stress–strain behaviour under uniaxial compression of alkali-activated concretes have been developed in recent years and are also summarised in Table 1. Hardjito et al. [39] evaluated the stress–strain response of heat-cured fly

ash-based alkali-activated concrete and demonstrated that the model proposed by Collins et al. [40] for PCC predicts quite accurately both the ascending and descending branch of the experimental curves. Noushini et al. [41] investigated the compressive response of heat-cured alkali-activated fly ash-based concrete and proposed new material parameters to better predict the ascending and descending branches of the stress–strain curve. Cong et al. [42] analysed the compressive stress–strain response of blended alkali-activated fly ash-slag concrete and proposed new analytical equations fitting the experimental stress–strain curves. Despite the current availability of analytical equations describing the stress–strain response of alkali-activated fly ash-based concretes, models to predict the compressive stress–strain behaviour of AASC with the incorporation of steel fibres are still missing. Although several studies investigated the performance of alkali-activated slag-based concrete reinforced with steel fibres, only a few focused on the full-range stress–strain response under uniaxial compression without providing any analytical model [21, 43].

The present study fills the research gap highlighted above and provides an in-depth understanding of the mechanical behaviour under uniaxial compression of alkali-activated slag-based concrete incorporating single and multiple hooked-end steel fibres in different volume fractions up to 0.75%. The compressive behaviour of the plain and fibre-reinforced AASC was characterised by the compressive strength, modulus of elasticity and stress–strain response under uniaxial compression. The same tests are also performed on traditional PCC reinforced with the same fibre types and contents to better evaluate the behaviour of different fibre geometries in different concrete matrices. The experimental results obtained for FRPCC, in combination with available literature data for steel FRPCC and FRAASC, have been used to propose and calibrate a new analytical model. This model can predict the stress–strain response of both AASC and PCC incorporating steel fibres, considering the matrix compressive peak stress and corresponding strain and the fibre reinforcing index RI_v as the only input parameters. The experimental data collected for FRAASC in this study are then used to validate the model. This allows for the verification of the suitability of the proposed model to any fibre and concrete

type and, in particular, to AASC reinforced with single and multiple hooked-end steel fibres.

2 Experimental programme

2.1 Materials

2.1.1 GGBS

The ground granulated blast furnace slag (GGBS) used in this study was supplied by the Dutch company Ecocem Benelux B.V. Its chemical composition was obtained by X-ray fluorescence (XRF) as shown in Table 2. The basicity coefficient $K_b = (CaO + MgO)/(SiO_2 + Al_2O_3)$ and the hydration modulus $HM = (CaO + MgO + Al_2O_3)/SiO_2$), in % by mass, were 1.05 and 1.66, respectively.

2.1.2 Alkaline activators

The alkaline activator used was a combination of sodium silicate (*waterglass*), sodium hydroxide and water. Sodium silicate (SS) solution was a commercially available product supplied by the company Woellner with a specific gravity of 1.37 g/cm^3 and a silicate modulus $M_{s(SS)}$(the molar ratio of SiO_2 to Na_2O) of 3.4. The silicate modulus of the alkaline solution was adjusted by adding sodium hydroxide solution (NaOH with 50% solid content) to achieve $M_{s(sol)}= 0.5$ [mol/mol] and a total concentration of 5.3% of Na_2O (expressed as a percentage of the slag weight). Additional water was added to the alkaline solution to achieve a liquid/binder ratio of 0.48, [kg/kg], where both the extra water and the water included in the activators is considered as liquid component. The different components of the alkaline activator were pre-mixed 24 h prior casting to reduce the heat released by the exothermic reaction between sodium hydroxide and sodium silicate solutions [5, 8] and avoid flash setting.

2.1.3 Portland cement

Portland cement (PC) CEM I 42.5 R produced by HeidelbergCement with a specific surface of 319.8 m^2/kg and loss on ignition of 4.57% was used. The chemical composition is also shown in Table 2.

Table 2 Chemical and physical properties of GGBS and PC (% by mass)

Binder	CaO (%)	SiO$_2$ (%)	Al$_2$O$_3$ (%)	Fe$_2$O$_3$ (%)	MgO (%)	P$_2$O$_5$ (%)	K$_2$O (%)	Na$_2$O (%)	Specific gravity [kg/m^3]	Blaine fineness (m^2/kg)
GGBS	41.84	35.91	10.74	0.39	6.99	0.47	0.40	0.31	2856.7	488.1
PC	60.80	19.60	5.25	2.38	1.53	0.13	0.80	0.10	3033.3	319.8

2.1.4 Fine and coarse aggregates

Quartzite gravel from the river Rhine with different maximum sizes, i.e. 8 mm and 16 mm, were used as fine and coarse aggregates, respectively. Natural river sand with a maximum size of 2 mm was also used.

2.1.5 Hooked-end steel fibres

Glued single and multiple hooked-end steel fibres, commercially available with the name of Dramix® 3D 65/60 BG, Dramix® 4D 65/60 BG and Dramix® 5D 65/60 BG, were supplied by NV Bekaert SA. The fibre geometry and properties are shown in Fig. 1 and Table 3, respectively. The three different fibre types used in this study have the same length (60 mm) and aspect ratio ($l_f/d_f = 65$) and differ from each other in terms of fibre tensile strength ($\sigma_{f,u}$) and the number of bends at the fibre hooked ends.

2.2 Mix proportions

AAS and PC concrete were designed to achieve the same strength and workability class, i.e. similar 28-day cubic mean compressive strength of 50 MPa (C35/45) and consistency class (F3-F4). The mix proportions for both AASC and PCC are shown in Table 4. To better assess the effect of hooked-end steel fibres in the different concrete matrices, the same binder content and aggregates type and proportions have been used for both AASC and PCC. Each fibre type has been added to the reference mixture of

Table 4 in different volume fractions, i.e. 0.25% (20 kg/m^3), 0.50% (40 kg/m^3) and 0.75% (60 kg/m^3).

A total of 20 mixes, 10 for each binder type, have been investigated. The matrix type (AASC or PCC), the fibre geometry (3D, 4D or 5D) and the fibre volume fraction (0.25%, 0.50% and 0.75%) define each mix. For example, the mix AASC-4D50 refers to the alkali-activated slag-based concrete reinforced with 4D fibres in a volume fraction of 0.50%. The plain concrete without fibres is referred as reference (REF).

2.3 Specimen preparation

To allow a better comparison between AASC and PCC mixes, the same casting procedure has been used. First, sand, fine and coarse aggregates and binder were dry-mixed in a 250-L concrete mixer for 90 s. The liquid component (the alkaline solution or water, for AASC and PCC, respectively) was then added and mixed for additional 2 min. Finally, steel fibres were added, and the mixing further prolonged up to a total of 7 min, to achieve homogeneous fibre distribution in the fresh concrete. The final mixture was then poured into the moulds. For each mixture, 9 cylinders with diameter of 150 mm and height of 300 mm and 3 cubes of 150 mm dimensions were prepared. To avoid segregation of both aggregates and fibres in the samples, the moulds were filled in a single layer and compacted on a vibrating table for 20 s at 40 Hz. The specimen were demoulded 24 h after casting and cured according to the binder type. PCC samples were cured underwater (20 ± 2 °C) for 27 days, while AASC specimens were wrapped in foil and placed in a

Fig. 1 Configurations of the different hooked-end steel fibres: **a** double bend (3D), **b** triple bend (4D), and **c** quadruple bend (5D). Arrows show the number of fibre bends

Table 3 Hooked-end steel fibres properties

Fibre type	Length (l_f) (mm)	Diameter (d_f) (mm)	Aspect ratio (l_f/d_f)	Fibre tensile strength ($\sigma_{f,u}$)[a] (MPa)	Strain at ultimate strength[a] (%)
3D 65/60 BG	60	0.90	65	1160	0.8
4D 65/60 BG	60	0.90	65	1600	0.8
5D 65/60 BG	60	0.90	65	2300	6.0

[a]Provided by NV Bekaert SA [45]

Table 4 Mix proportions of AASC and PCC

	GGBS (kg/m^3)	CEM I (kg/m^3)	Sodium hydroxide (kg/m^3)	Sodium silicate (kg/m^3)	Water (kg/m^3)	Sand (0–2 mm) (kg/m^3)	Fine aggregates (2–8 mm) (kg/m^3)	Coarse aggregates (8–16 mm) (kg/m^3)
AASC	425	–	50	36	154	660	495	495
PCC	–	425	–	–	229	660	495	495

climate room at (20 ± 2) °C and 65% relative humidity until testing date. Underwater curing should be prevented for alkali-activated concrete mixtures to avoid the leaching effect of alkalis in water [19].

2.4 Testing procedure

The effect of hooked-end steel fibres on the compressive behaviour of AASC and PCC is evaluated by the 28-day compressive strength, modulus of elasticity and stress–strain response under uniaxial compression. To guarantee uniform distribution of the compressive load between the sample surfaces and the testing machine plates, both top and bottom surfaces were ground the day before the testing date.

Three cubes and three cylinders were then tested to evaluate the 28-day mean compressive strength according to EN 12390–3. The modulus of elasticity was determined on three cylindrical samples according to EN 12390–13:2014 (part B), and three additional cylinders have been used to investigate the stress–strain response under compression.

The stress–strain behaviour under compression was evaluated using an MTS compression-tension testing machine with 2500 kN capacity with a constant loading head displacement rate of 0.30 mm/min. The presence of a spherical calotte above the upper plate of

the machine guarantees that the load is always applied in the centre of the sample surface, avoiding load eccentricity. Four external linear variable differential transformers (LVDTs) were installed between both ends of the specimens, as shown in Fig. 2, to assess the axial plate-to-plate deformation and evaluate the post-peak stress–strain response up to a strain value of 0.01 (10‰).

The plate-to-plate strain measurement can lead to higher strain values in the pre-peak region compared to mid-span deformation measurement, although it is not disturbed by the cracking of the sample surfaces. This results in a better reading of the post-peak descending branch [46, 47], where the effect of hooked-end steel fibres on the compressive response is more pronounced. Therefore, axial plate-to-plate deformation measurements were chosen in this study.

Figure 3a shows a generic stress–strain curve obtained experimentally as the average of three cylindrical samples. The non-linearity at the origin (in the red circle) is usually due to the specimen versus testing machine stiffness and micro-cracking at the aggregate-matrix interfaces [36].

Due to the test setup, it is not possible to derive from the stress–strain curve the modulus of elasticity E_0. The modulus of elasticity is typically calculated by measuring the deformation in the central zone of a
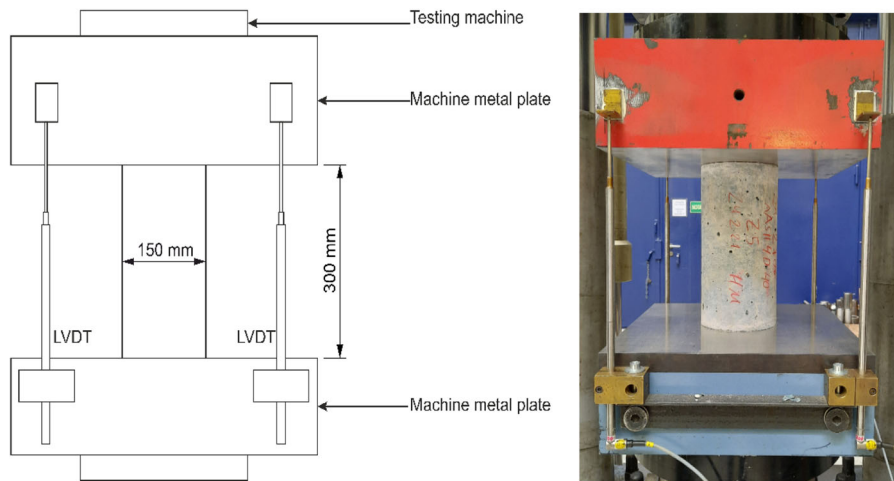
Fig. 2 Test set-up to evaluate the stress–strain response under uniaxial compression
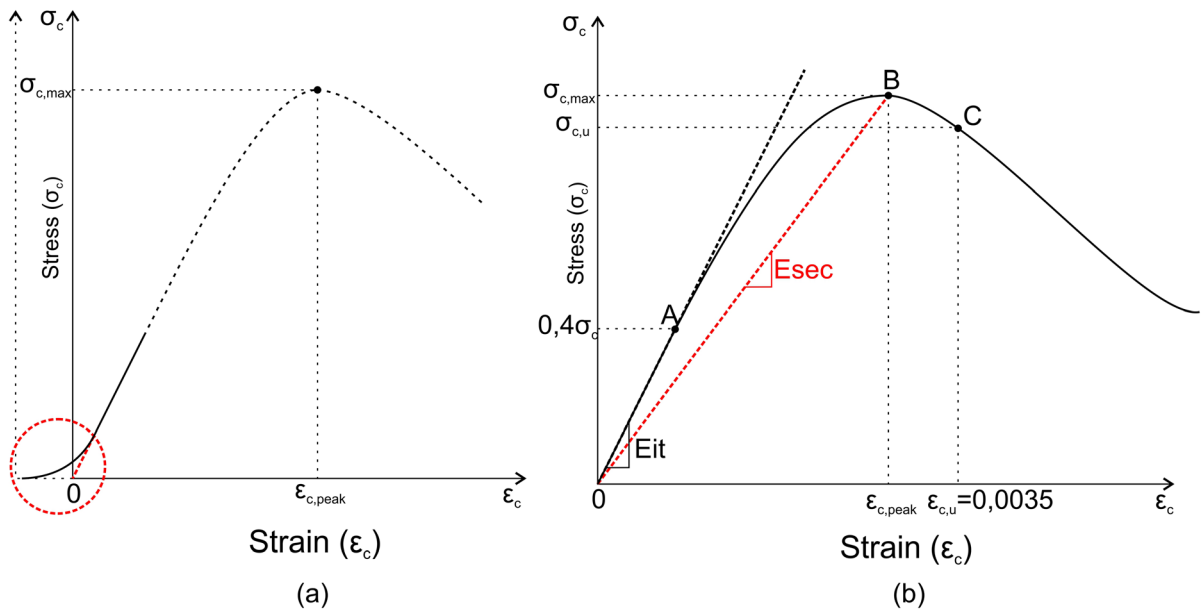
Fig. 3 General experimental stress–strain curve obtained as an average of three samples **a** and **b** definition of the compressive parameters E_{it} (initial secant modulus at 40% of the peak stress) and E_{sec} (secant modulus)

loaded cylinder, which is widely assumed to be subjected to a near-uniform uniaxial compressive stress due to the negligible frictional restraint at the specimen-plate interfaces [48]. When measuring the deformation of the central zone of the sample under uniaxial compression, the modulus of elasticity E_0 can be derived from the experimental stress–strain curve as the slope of the linear section 0A (Fig. 3b). However, measuring the plate-to-plate deformation results in an underestimation of the modulus of

elasticity, due to the frictional restraints and resulting complex state of compressive stresses at the end of the sample [48]. Thus, for comparison purpose, the parameters E_{it} and E_{sec}, i.e. the initial secant modulus and the secant modulus, respectively, are defined for each experimental average stress–strain curve. The initial secant modulus represents the slope the linear region OA up to a stress corresponding to 40% of the peak stress. The secant modulus is defined as the slope of the line connecting the origin with the maximum

stress (OB). From the definition of E_0, E_{it} and E_{sec}, it is clear that $E_0 > E_{it} > E_{sec}$.

3 Results

3.1 Compressive strength and modulus of elasticity

Figure 4 shows the mean compressive strength of both cubic and cylindrical samples and the modulus of elasticity for AASC reinforced with 3D, 4D and 5D fibres at 0%, 0.25%, 0.50% and 0.75% fibre volume fractions. AASC mixes incorporating hooked-end steel fibres show enhanced cubic and cylindrical compressive strength compared to the reference unreinforced mix, regardless of fibre geometry and volume fraction.

However, the increase in compressive strength provided by fibre incorporation is not directly correlated to the fibre volume fraction, as the highest values of strength are not always achieved at the highest fibre dosage for each fibre type. Only for 3D fibres, the mix incorporating the highest fibre volume fraction achieves the highest compressive strength values of 55.8 MPa and 48.3 MPa for cubes and cylinders, respectively. For 4D and 5D fibres, the highest values of compressive strength are obtained for the mixes

AASC-4D25 and AASC-5D50, respectively. The effects of fibre content on the compressive strength of composites reinforced with different fibre types can be correlated to the distribution and orientation of the fibres in the samples [49]. Fibres aligned perpendicular to the crack opening in the stress direction can lead to higher values of compressive strength [13] due to the fibre crack bridging and stress transferring effect. As shown in Fig. 4a, both cubic and cylindrical samples show similar strength variations with the increase of the fibre volume fraction for each fibre type. The highest values of cubic and cylindrical compressive strength, 57.8 MPa and 52.6 MPa, respectively, are achieved by the mix AASC-5D50, corresponding to an increase in strength in comparison to the strengths of the reference mix of 21.8% and 28.6%, respectively. Despite the similar trend observed for the cubic and cylindrical compressive strength of FRAASC, the conversion factor correlating the cubic to the cylindrical compressive strengths differs with the fibre geometry. The correlation between cubic and cylindrical compressive strength for each fibre type and volume fraction is evaluated and discussed in the supplementary information.

Figure 4b shows the 28-day mean modulus of elasticity of AASC mixes reinforced with 3D, 4D and 5D fibres in different fibre volume fractions. The incorporation of hooked-end steel fibres enhances the
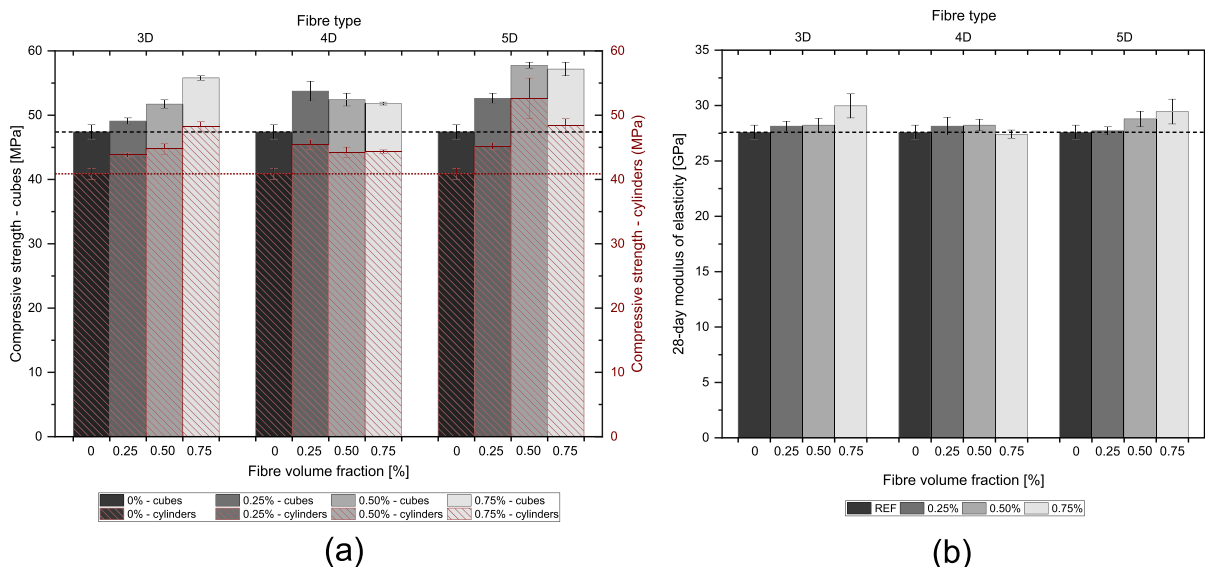
Fig. 4 28-day mean cubic and cylindrical compressive strength **a** and modulus of elasticity **b** of AASC reinforced with 3D, 4D and 5D steel fibres in different volume fractions

modulus of elasticity of the plain matrix, regardless of the fibre geometry and volume fraction. The modulus of elasticity increases with the increase of the fibre volume fraction, regardless of the fibre type. The slight increment of the modulus of elasticity with the incorporation of steel fibres up to 1% volume fraction can be attributed to the high stiffness of the fibres and the strong fibre-matrix interaction [14, 50]. The mix AASC-4D75 is the only exception in the present study. The decrease of the modulus of elasticity with the increase of the fibre volume fraction from 0.50 to 0.75% can be due to fibre distribution and orientation, which affect the porosity of the composite [14, 50], resulting in a negative effect on the modulus of elasticity.

3.2 Stress–strain behaviour under uniaxial compression

The compressive stress–strain response of fibre-reinforced alkali-activated concrete is linear and similar to that of plain concrete up to a stress corresponding to around 40% of the peak stress, as shown in Fig. 5. Micro-cracks start forming and propagating as the stresses increase, marginally activating the crack-bridging capacity of the hooked-end steel fibres. However, steel fibres have a minimal effect on the pre-peak ascending branch of the stress–strain curve, regardless of the fibre geometry and volume fraction. As stresses approach the maximum stress $\sigma_{c,max}$, the isolated micro-cracks formed start propagating in an unpredictable way, due to the material inhomogeneity and the presence of fibres, leading to the formation of several macro-cracks. For the unreinforced mixture,

once the maximum compressive stress is reached, the load-bearing capacity of the material decreases rapidly, resulting in a quasi-brittle behaviour corresponding to a steep post-peak descending branch of the diagram. Fibre-reinforced mixtures exhibit a softer post-peak descending branch as a result of the transverse confinement effect of the hooked-end steel fibres [38].

Figure 5 shows the experimental stress–strain curves obtained for AASC reinforced with 3D, 4D and 5D fibres in different volume fraction. The incorporation of hooked-end steel fibres, regardless of the fibre geometry and volume fraction, enhances both the peak stress ($\sigma_{c,max}$) and corresponding strain ($\varepsilon_{c,max}$) of the composites in comparison to the reference concrete, as also shown in Fig. 6a, b.

The compressive peak stress increment has no clear correlation to the fibre content variation, but it follows the same trend observed for the compressive strength as shown in Fig. 4a. The corresponding peak strain increases with the increase of the fibre volume fraction, achieving the highest values at the highest fibre volume fraction, regardless of the fibre geometry. The incorporation of hooked-end steel fibres at a volume fraction of 0.75% enhances the compressive peak strain of the plain matrix by 22.5%, 28.8% and 21.6%, for 3D, 4D and 5D fibres, respectively. The increase in value of $\varepsilon_{c,max}$ leads to a reduction of the initial secant modulus E_{it} and the secand modulus E_{sec} in comparison to the reference mix, as shown in Fig. 6c. However, the increased strain corresponding to the peak stress coupled with the softer post-peak descending branch of the stress–strain response

(a)   (b)   (c)
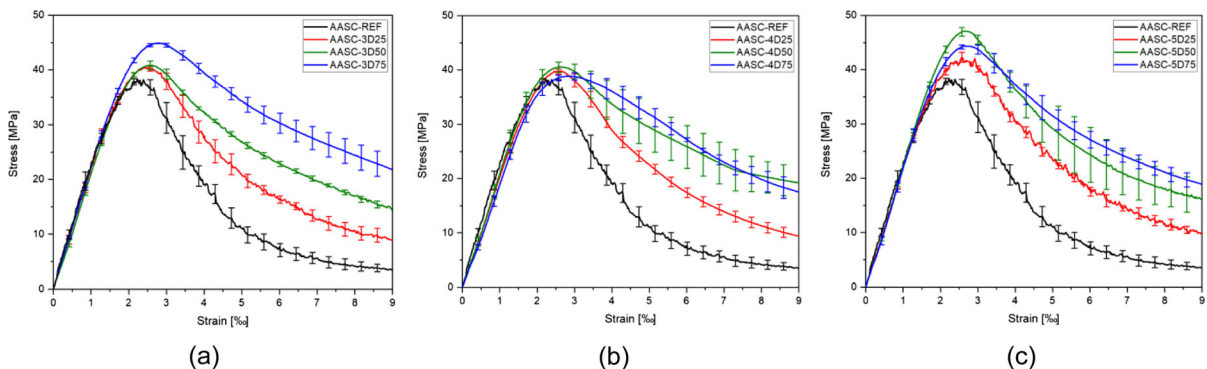
Fig. 5 Experimental stress–strain curves obtained for AASC reinforced with **a** 3D fibres, **b** 4D fibres and **c** 5D fibres in different fibre volume fractions
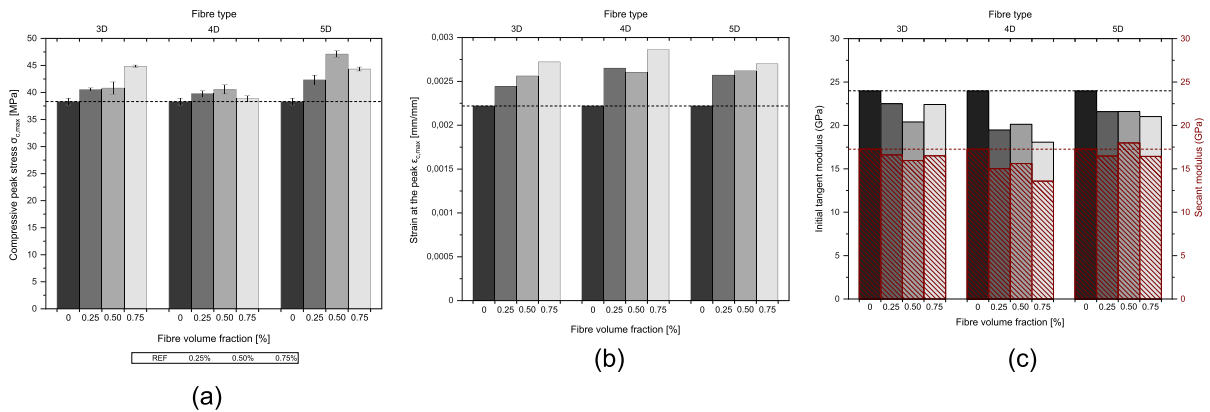
Fig. 6 Effect of fibre geometry and content on **a** the compressive peak stress, **b** the strain at the peak and **c** the secant and initial secant moduli

demonstrates the improved ductility of the material when reinforced with hooked-end steel fibres.

3.3 Comparison with fibre-reinforced Portland cement concrete (FRPCC)

3.3.1 Compressive strength and modulus of elasticity

Figure 7a shows the cubic and cylindrical compressive strength of PCC mixes reinforced with different hooked-end steel fibres at different fibre volume fractions. Although the PCC reference mix shows similar mean cubic compressive strength as AASC, 49.46 MPa and 47.40 MPa, respectively, the incorporation of hooked-end steel fibres shows a different behaviour in the two matrix types. In contrast to FRAASC (see Fig. 4a), hooked-end steel fibres have a limited effect on the compressive strength of PCC. AASC mixes show an increment of strength in comparison to the reference mix up to 21.8% (AASC-5D50), while PCC mixes achieve a maximum increment of only 1.54% (PCC-5D75). A similar
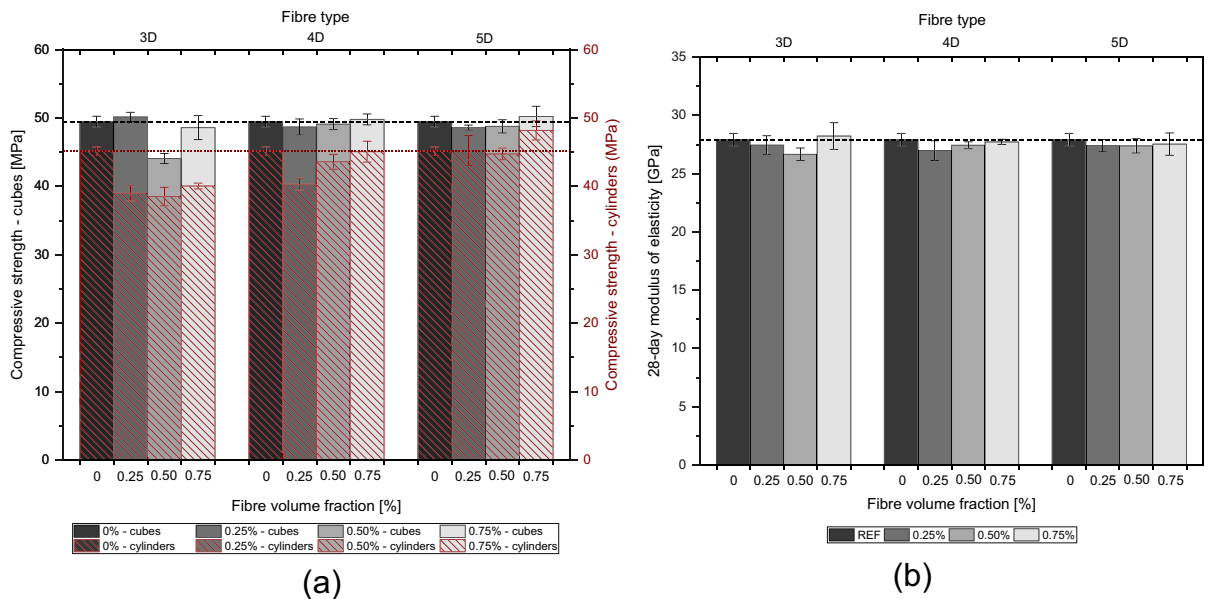
Fig. 7 28-day mean cubic and cylindrical compressive strength **a** and modulus of elasticity **b** of PCC reinforced with 3D, 4D and 5D steel fibres in different volume fractions

behaviour for PCC was reported also by Lee et al. [27], in which the incorporation of 3D, 4D and 5D fibres does not significantly affect the compressive strength values up to a volume fraction of 1%.

Beglarigale et al. [51] demonstrated that alkali-activated slag composites reinforced with hooked-end steel fibres exhibit superior bond strength compared to traditional PCC. The improved fibre-matrix interaction can be attributed to the higher shrinkage behaviour of AASC in comparison to PCC. The higher shrinkage in AASC matrix generates a hydrostatic pressure around the fibre, improving the fibre-matrix bond [51]. In addition, the stresses generated by the shrinkage-induced micro-cracking provide an early activation of the steel fibres, resulting in improved mechanical performance of AASC when compared to PCC. As for FRAASC (Sect. 3.1), the correlation between cubic and cylindrical compressive strength of PCC reinforced with single and multiple hooked-end steel fibres is evaluated and discussed in the supplementary information.

Figure 7b shows the 28-day mean modulus of elasticity of PCC mixes reinforced with single and multiple hooked-end steel fibres in different volume fractions. Although the PCC-REF mix shows similar modulus of elasticity as AASC-REF, 27.91 GPa and 27.58 GPa, respectively, hooked-end steel fibres have a different effect on the two matrices. For AASC, the modulus of elasticity increases with the increase of the fibre volume fraction (Fig. 4b), with AASC-3D75 achieving the highest value of 29.96 GPa (+ 8.6% than AASC-REF). For PCC mixes, the incorporation of steel fibres leads to a reduction of the modulus of elasticity in comparison to the reference mix, with only the PCC-3D75 mix showing an increase of 1.15%. The modulus of elasticity is mainly dependent on the coarse aggregate type and content and the compressive strength of the matrix, with fibres playing a minor role [52]. However, hooked-end steel fibres have a more positive effect on the modulus of elasticity of AASC than PCC. As the coarse aggregates type and amount is kept constant in AASC and PCC mixtures, the increase of modulus of elasticity provided by the hooked-end steel fibres in AASC composites can be related to the enhanced compressive strength of the composite caused by the stronger fibre-matrix bond and to the higher shrinkage of the AASC matrix in comparison to traditional concrete [51], as previously explained.

3.3.2 Stress–strain under uniaxial compression

Figure 8 shows the experimental stress–strain curves obtained for PCC mixtures reinforced with 3D, 4D and 5D fibres in different volume fractions and the direct comparison with AASC. Hooked-end steel fibres have a limited effect on the compressive peak stress and corresponding peak strain of PCC composites, with only the mixtures reinforced with 0.75% fibre volume fraction showing minimal improvements. For lower fibre contents the fibre incorporation has a negligible or even negative effect on these parameters in comparison to the reference plain concrete. However, a significant enhancement of the residual stress at higher strain values can be seen for PCC matrix for all the fibres types, with the higher fibre volume fraction and fibre bends providing the highest residual compressive stress at ultimate strain, corresponding to a softer post-peak descending branch in the stress–strain diagram.

Figure 9a, c show the correlations between the peak stress and the corresponding strain of both PCC and AASC mixes with the fibre reinforcing index RI_v, respectively. Although the peak compressive stress increases with the increase of the fibre reinforcing index from 0.167 to 0.50 (Fig. 9a) for both AASC and PCC, AASC mixes show higher values than PCC, regardless of the fibre geometry. When the strain corresponding to the peak stress is considered (Fig. 9c), PCC mixes show higher values than AASC at $RI_v = 0.50$. However, to evaluate the contribution of hooked-end steel fibres on the compressive stress–strain response of both AASC and PCC mixes, the $\sigma_{c,max(FRC)}/\sigma_{c,max(REF)}$ and the $\varepsilon_{c,max(FRC)}/\varepsilon_{c,max(REF)}$ ratios need to be considered. $\sigma_{c,max(FRC)}/\sigma_{c,max(REF)}$ represents the ratio between the peak stress of the mix incorporating steel fibres ($\sigma_{c,max(FRC)}$) and the peak stress of the reference concrete ($\sigma_{c,max(REF)}$), while $\varepsilon_{c,max(FRC)}/\varepsilon_{c,max(REF)}$ represents the ratio of the value of the strain corresponding to the peak stress of fibre-reinforced and reference mixes, respectively. As shown in Fig. 9b, hooked-end steel fibres have a positive effect on the compressive peak stress of AASC, as the $\sigma_{c,max(FRC)}/\sigma_{c,max(REF)}$ ratio is higher than 1, regardless of the fibre geometry and reinforcing index. For PCC mixes, only the mixes containing 4D and 5D fibres in volume fractions higher than 0.25% show values of $\sigma_{c,max(FRC)}/\sigma_{c,max(REF)}$ higher than 1.
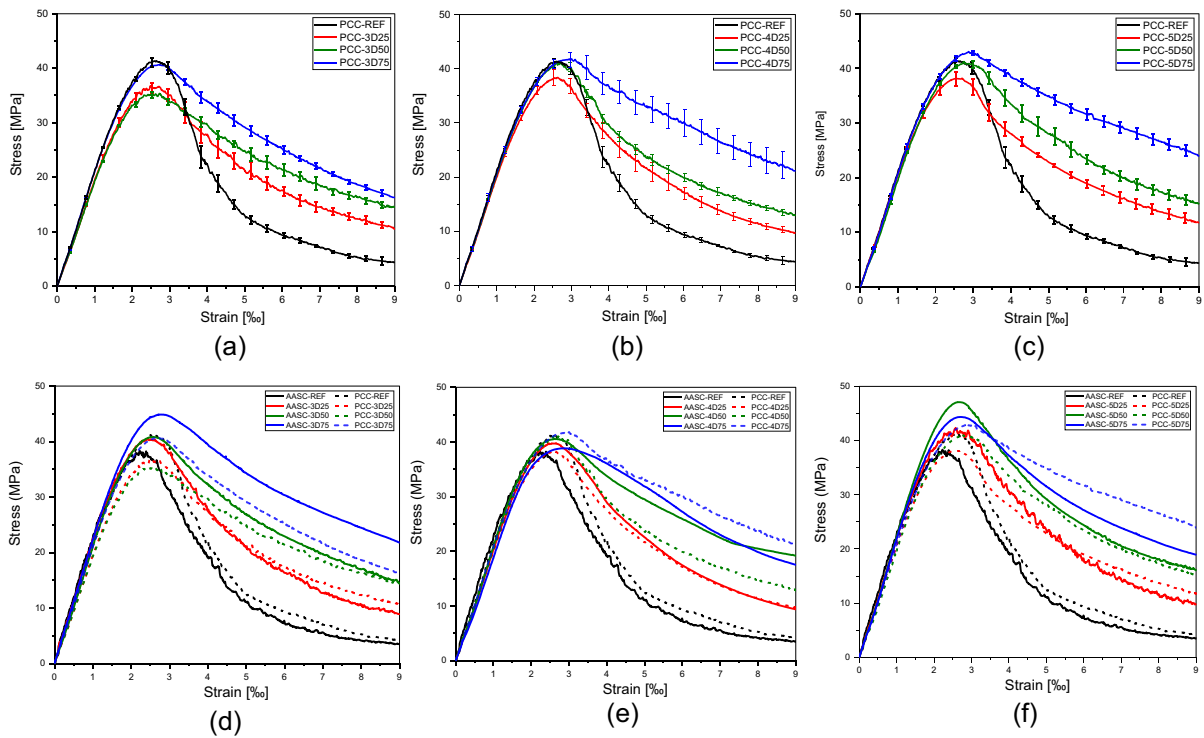
Fig. 8 Experimental stress–strain curves of PCC mixes reinforced with **a** 3D, **b** 4D and **c** 5D hooked-end steel fibres in different volume fractions and direct comparison with AASC reinforced with **d** 3D, **e** 4D and **f** 5D fibres

The incorporation of 3D fibres in volume fractions up to 0.75% has no beneficial effect on the compressive peak stress of the PCC matrix.

As shown in Fig. 9d, the incorporation of hooked-end steel fibres has a beneficial effect on the compressive strain corresponding to the peak stress, as the value of the ratio between the strain corresponding to the peak of the mixes incorporating steel fibres and the reference mix ($\varepsilon_{c,max(FRC)}/\varepsilon_{c,max(REF)}$) is higher than 1 for both PCC and AASC, regardless of the fibre geometry and volume fraction. However, in comparison to PCC, AASC mixes show a higher increment of strain corresponding to peak stress in comparison to the reference matrix when steel fibres are added, indicating a higher ductility. The higher ductility of the steel fibre-reinforced AASC mixes in comparison to PCC can be better seen in Fig. 9e, f. The value of the stress corresponding to the ultimate strain of 0.0035 ($\sigma_{c,u(FRC)}$) (Fig. 9e) gives an indication of the slope of the post-peak descending branch of the stress–strain curve, where higher values of $\sigma_{c,u(FRC)}$ correspond to softer descending curves and higher ductility. To isolate the effect of fibre geometry

and reinforcing index on the ductility of the composite, the values of $\sigma_{c,u(FRC)}$ are normalised to the values of the reference mix ($\sigma_{c,u(REF)}$) and are shown in Fig. 9f. Although the values of the $\sigma_{c,u(FRC)}/\sigma_{c,u(REF)}$ ratio are higher than 1 for both AASC and PCC, AASC mixes show a higher increment of ductility in comparison to the reference mix for each fibre type and volume fraction than PCC.

4 Analytical modelling of the stress–strain behaviour

4.1 Model description and calibration

Currently available models to predict the stress–strain under uniaxial compression of fibre-reinforced concrete (Table 1) cannot be applied to PCC and AASC reinforced with single and multiple hooked-end steel fibres. This is because these models are derived and calibrated using a limited number of experimental data and they are strictly dependent on the fibre type, dosage and matrix strength investigated. Furthermore,
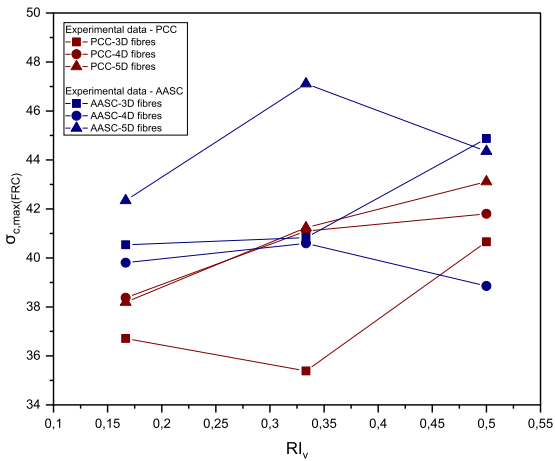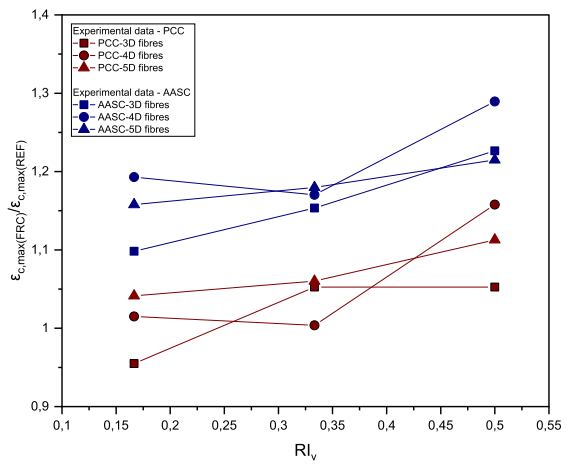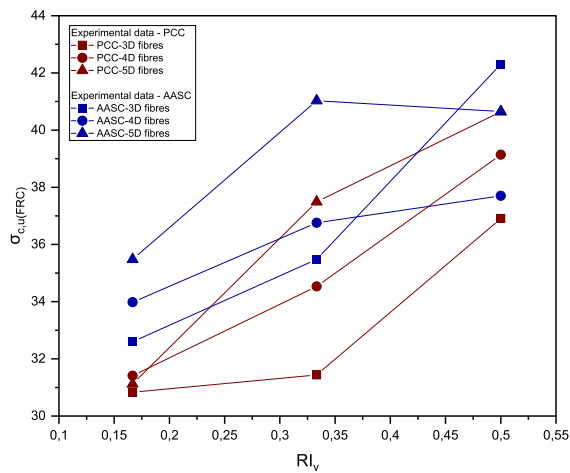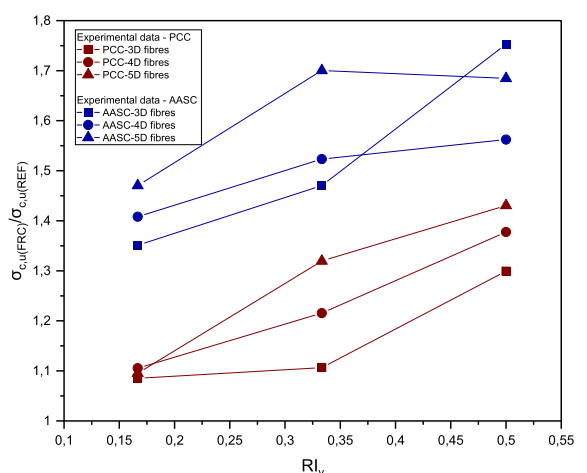
(a)
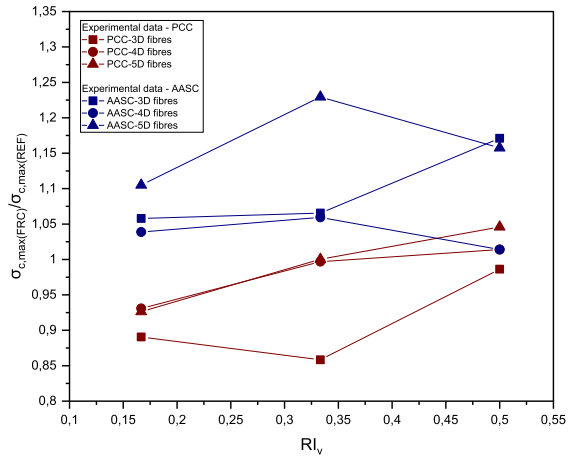
(b)
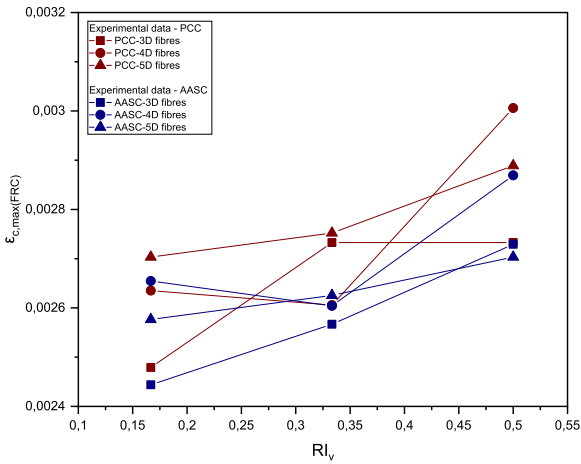
(c)

(d)

(e)

(f)

most of the available models are based on a single equation, neglecting the difference in the effect of steel fibres incorporation on the pre-and post-peak response of the compressive stress–strain curves. This provides an overestimation of the compressive behaviour in both the pre- and post-peak phases.

Figure 10 shows the experimental stress–strain curves obtained for the plain AASC and the mixes reinforced with 3D, 4D and 5D fibres at 0.75% fibre volume fraction and the predicted curves obtained applying the models developed to alkali-activated concrete (Table 1). The model developed by Hardjito et al. [39] can predict the response of plain alkali-activated slag-based concrete quite accurately (Fig. 10a), while the models proposed by Noushini et al. [41] and Cong et al. [42], highly under- or overestimate, respectively, the post-peak descending branch of the curve. However, all the models are unable to predict the post-peak behaviour of AASC incorporating single and multiple hooked-end steel fibres, as shown in Fig. 10b–d, as the
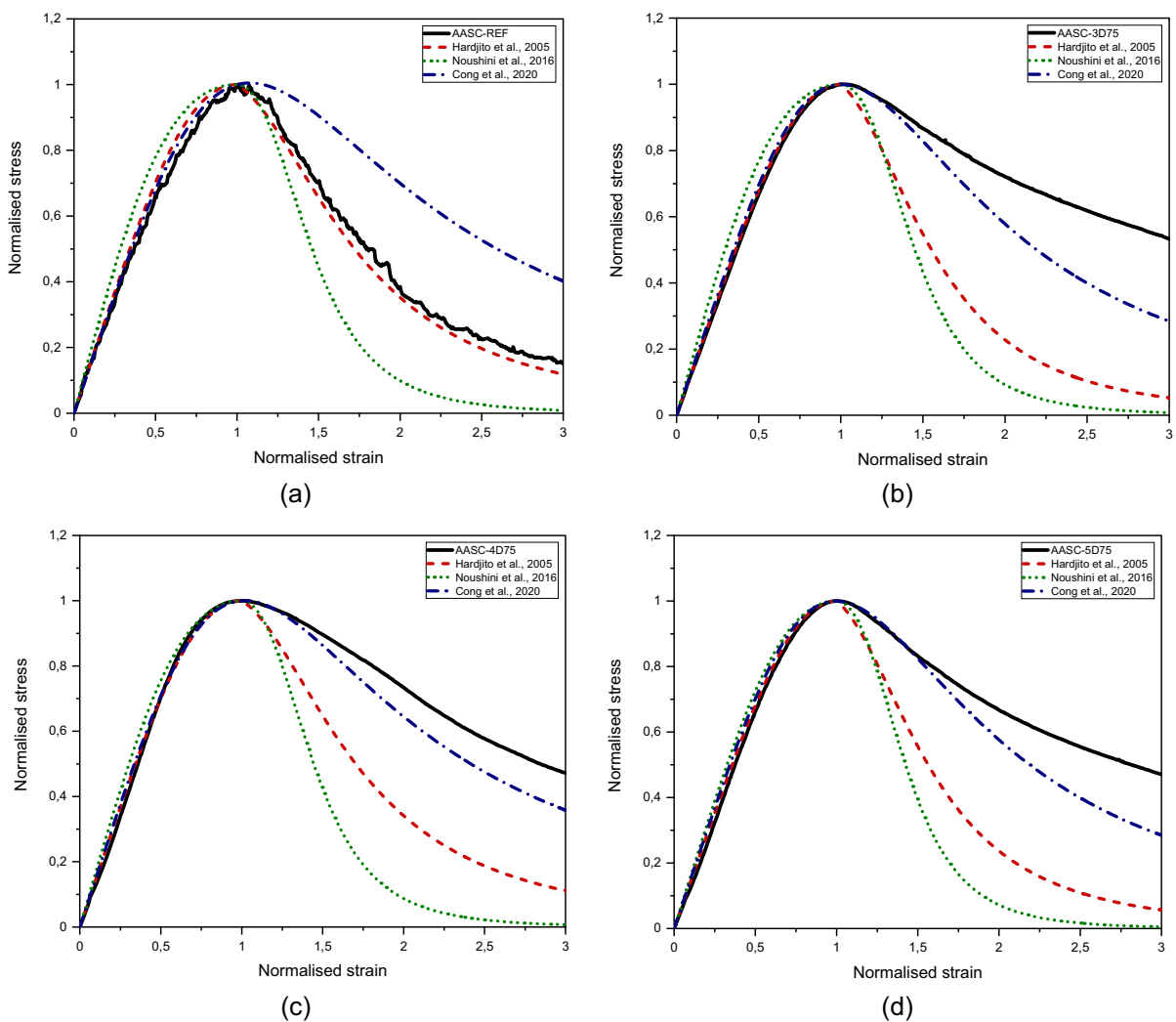
Fig. 10 Experimental and predicted stress–strain curves according to current models developed for alkali-activated concrete for **a** AASC-REF, **b** AASC-3D75, **c** AASC-4D75 and **d** AASC-5D75
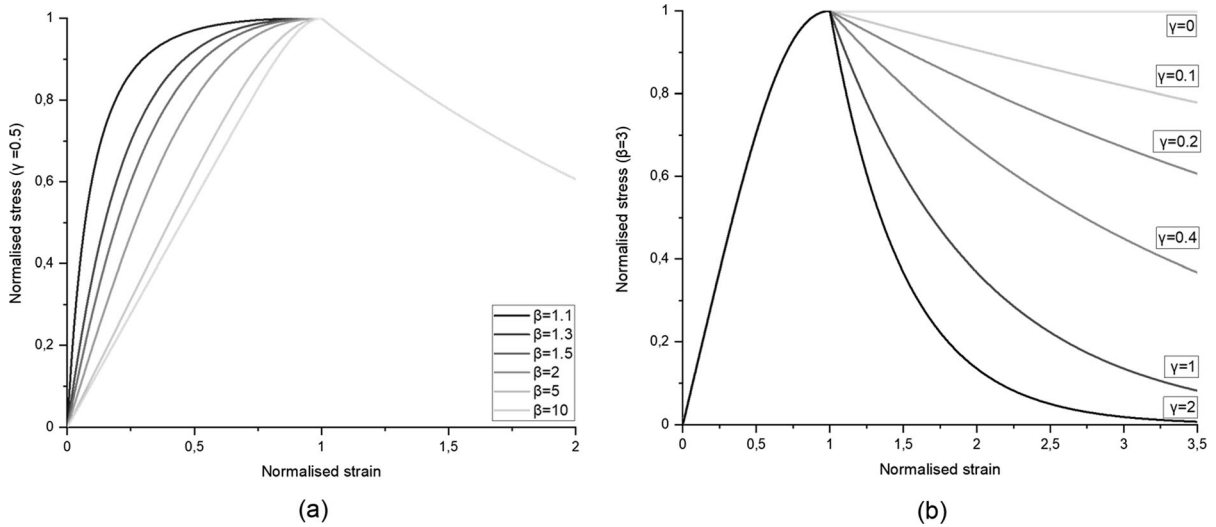
Fig. 11 Effect of the material parameters **a** β and **b** γ on the compressive stress–strain curve of fibre-reinforced concrete
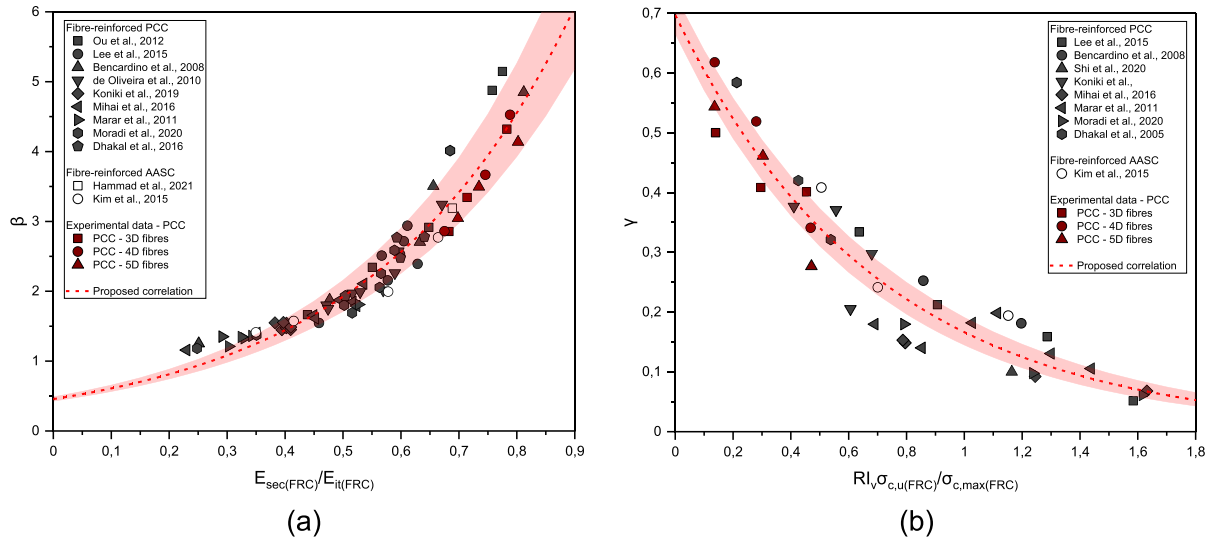
Fig. 12 Proposed correlations to derive the values of **a** β and **b** γ. The shaded areas represent the 95% confidence interval of the parameters of Eq. (3) and (4), respectively

effect of fibre incorporation is not considered in these models.

For this reason, a new analytical model is proposed, which describes the normalised ascending and descending branches of the stress–strain curve through two analytical expressions. In the proposed model, the pre-peak response is based on the function proposed by Ezeldin and Balaguru [35]. The post-peak descending branch is modelled using an exponential decay equation, which has been commonly used in the past to
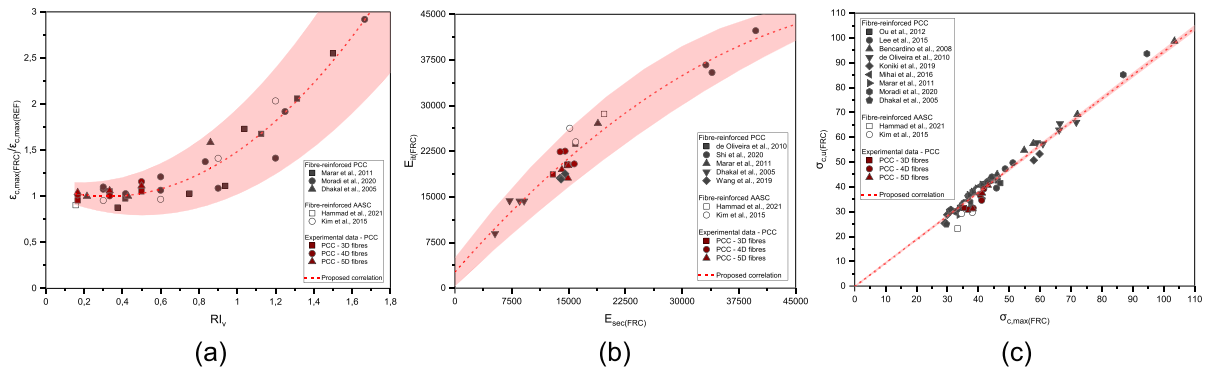
describe the post-cracking softening behaviour of unreinforced concrete [53]. The final analytical expression of the proposed model is given in Eq. 2.

$$
\frac{\sigma_c}{\sigma_{c,\max(\mathrm{FRC})}} = \begin{cases} \dfrac{\beta\left(\varepsilon_c/\varepsilon_{c,\max(\mathrm{FRC})}\right)}{\beta - 1 + \left(\varepsilon/\varepsilon_{c,\max(\mathrm{FRC})}\right)^{\beta}} & \varepsilon/\varepsilon_{c,\max(\mathrm{FRC})} \le 1 \\[4mm] e^{\gamma\left(1 - \varepsilon_c/\varepsilon_{c,\max(\mathrm{FRC})}\right)} & \varepsilon/\varepsilon_{c,\max(\mathrm{FRC})} > 1 \end{cases}
$$
(2)

where σ_c is the compressive stress and ε_c is the corresponding strain, $\sigma_{c,\max(\mathrm{FRC})}$ is the maximum

Fig. 13 Proposed correlations to derive the values of **a** $\varepsilon_{c,max(FRC)}$, **b** $E_{it(FRC)}$ and **c** $\sigma_{c,u(FRC)}$. The shaded areas represent the 95% confidence interval of the parameters of Eqs. (7), (8) and (9), respectively

compressive stress of the composite and $\varepsilon_{c,max(FRC)}$ is the corresponding peak strain, β and γ are material parameters governing the pre-peak and post-peak behaviour, respectively, as shown in Fig. 11. The parameter β controls the ascending pre-peak branch of the stress–strain curve, where fibres play a minimal role. Hence the parameter β is only dependent on the ratio between the secant modulus E_{sec} and the initial secant modulus E_{it} of the composite. Increasing values of β corresponds to decreasing steepness of the ascending branch. The parameter γ governs the steepness of the post-peak descending branch. Values of γ increasing from the 0 to ∞ represent the variation

of material behaviour from perfectly plastic to brittle, respectively.

The proposed model was calibrated on a wide range of stress–strain curves available in the literature for steel fibre-reinforced PCC [32, 33, 38, 47, 54–60], AASC composites [21, 43] and the experimental results obtained in this study for PCC mixes reinforced with single and multiple hooked-end steel fibres. The objective function used for the model calibration is defined as the absolute value of the difference between the experimental data and the predicted values obtained applying the proposed model equations. Minimising this objective function provides the values of the parameter β and γ for each stress–strain curve
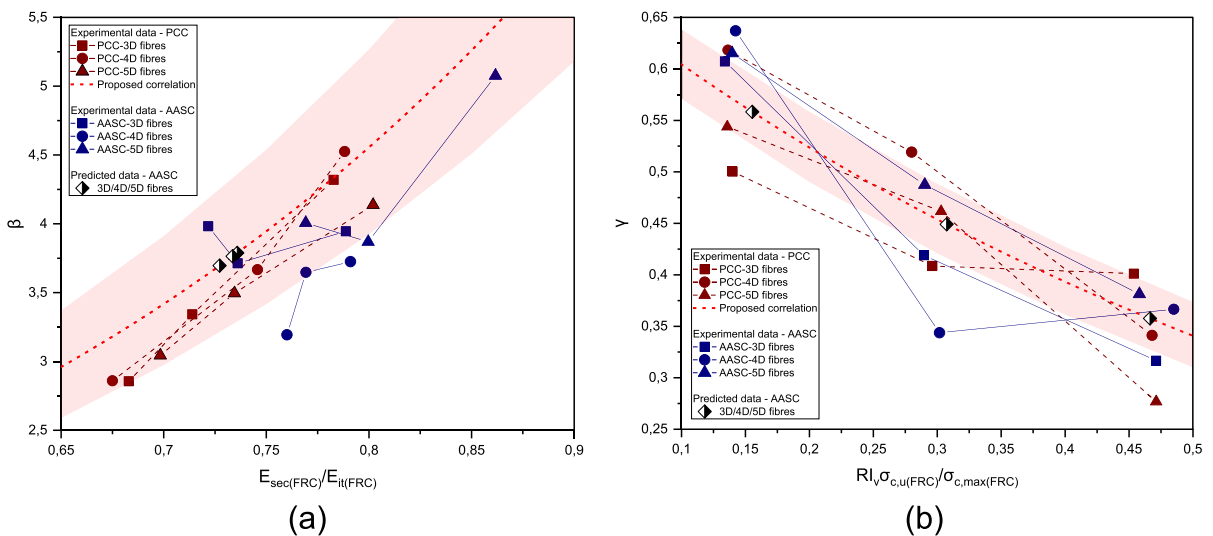
Fig. 14 Values of the parameters **a** β and **b** γ obtained by fitting the experimental data for both fibre-reinforced PCC and AASC and the predicted values of AASC used for the model validation.

The shaded areas represent the 95% confidence interval of the parameters of Eqs. (3) and (4), respectively

considered. The minimisation is carried out using the Generalised Reduced Gradient (GRG) non-linear optimisation algorithm available in the Microsoft Excel® Solver add-in. The collected values of β and γ were then correlated to the parameters governing the pre- and post-peak responses. These parameters are E_{it} and E_{sec} for the ascending branch, while for the descending branch the fibre reinforcing index (RI_v) and the ultimate stress corresponding to a strain of 0.0035, defined in the Eurocode 2 as the ultimate compressive strain in plain PCC ($\sigma_{c,u}$). The proposed correlations of the material parameters β and γ with E_{it}, E_{sec} and RI_v are defined by Eq. (3) and (4) and shown in Fig. 12.

$$\beta = (0.457 \pm 0.030)e^{(2.874 \pm 0.100)\left(E_{sec(FRC)}/E_{it(FRC)}\right)} \tag{3}$$
$$\left(R^2 = 0.926\right)$$

$$\gamma = (0.697 \pm 0.032)e^{(-1.432 \pm 0.092)\left(RI_v\sigma_{c,u(FRC)}/\sigma_{c,max(FRC)}\right)}$$
$$\left(R^2 = 0.901\right) \tag{4}$$

As shown in Fig. 12a, the values of the material parameter β obtained by fitting the proposed model to the stress–strain curves available in the literature for both steel fibre-reinforced PCC and AASC and the experimental curves obtained in this study for PCC fall in the range of the confidence interval of the proposed Eq. (3). Greater variability in the values of parameter γ can be seen in Fig. 12b. Finally, correlations can be established between $\sigma_{c,max(FRC)}$, $\varepsilon_{c,max(FRC)}$ and $E_{it(FRC)}$ of the steel fibre-reinforced composite and $\sigma_{c,max(REF)}$, $\varepsilon_{c,max(REF)}$ and $E_{it(REF)}$ of the reference concrete. These

correlations between unreinforced concrete and the fibre-reinforced composite are summarised below and shown in Fig. 13:

$$E_{sec(FRC)} = \sigma_{c,max(FRC)}/\varepsilon_{c,amx(FRC)} \tag{5}$$

$$\sigma_{c,max(FRC)} = \sigma_{c,max(REF)} + 4.8853RI_v \tag{6}$$
$$\left(R^2 = 0.935\right)$$

$$\varepsilon_{c,max(FRC)}/\varepsilon_{c,max(REF)} = 1.064RI_v^2 - 0.689RI_v$$
$$+ 1.109 \tag{7}$$
$$\left(R^2 = 0.915\right)$$

$$E_{it(FRC)} = -0.0000114E_{sec(FRC)}^2 + 1.418E_{sec(FRC)}$$
$$+ 2625.13$$
$$\left(R^2 = 0.929\right)$$
$$\tag{8}$$

Furthermore, the value of $\sigma_{c,u(FRC)}$ is defined as follows:

$$\sigma_{c,u(FRC)} = 0.9927\sigma_{c,max(FRC)} - 2.317 \tag{9}$$
$$\left(R^2 = 0.977\right)$$

Figure 13 shows the fitted correlations for $\varepsilon_{c,max(FRC)}$, $E_{it(FRC)}$ and $\sigma_{c,u(FRC)}$. Despite the limited amount of data for alkali-activated slag-based concrete available in the literature, the proposed correlations (Eqs. (6)–(9)) are able to capture the values obtained for both PCC and AASC reinforced with steel fibres, especially the values obtained experimentally for PCC reinforced with novel hooked-end steel fibres.

4.2 Model validation

Figure 14 shows the values of the parameters β and γ obtained by fitting the experimental stress–strain curves of both fibre-reinforced PCC and AASC and the predicted values of β and γ for fibre-reinforced AASC obtained by using the proposed model. Although the predicted values of $E_{sec(FRC)}/E_{it(FRC)}$ for fibre-reinforced AASC is slightly underestimated by the proposed correlation (Fig. 14a), the predicted values of β fall in the range of the fitted values, i.e. between 3.2 and 5.1.

Due to the lack of available experimental stress–strain curves for steel FRAASC, the fitted values of the parameter γ do not fall in the confidence interval proposed (Fig. 14b). Table 5 shows the fitted and

Table 5 Fitted and predicted values of the parameters β and γ for AASC mixes reinforced with 3D, 4D and 5D fibres

Mix	β-fitted	β-predicted	γ-fitted	γ-predicted
AASC-3D25	3.982	3.696	0.607	0.558
AASC-3D50	3.713	3.789	0.419	0.449
AASC-3D75	3.946	3.764	0.317	0.358
AASC-4D25	3.194	3.696	0.637	0.558
AASC-4D50	3.648	3.789	0.344	0.449
AASC-4D75	3.725	3.764	0.366	0.358
AASC-5D25	4.007	3.696	0.615	0.558
AASC-5D50	3.870	3.789	0.487	0.449
AASC-5D75	5.077	3.764	0.381	0.358
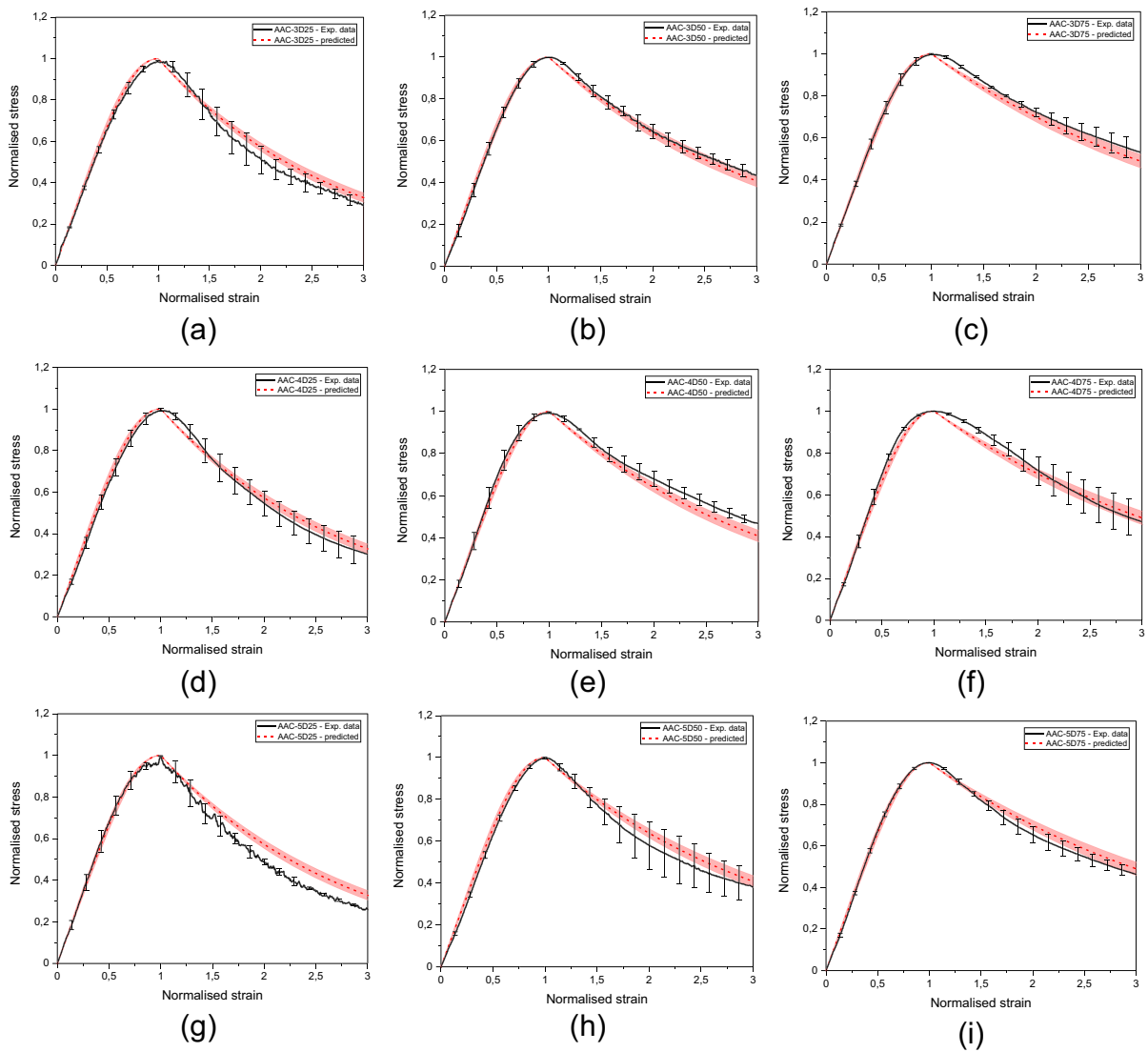
Fig. 15 Experimental and predicted stress–strain curves for AASC reinforced with **a–c** 3D, **d–f** 4D and **g–i** 5D fibres in different volume fractions. The shaded areas represent the 95% confidence interval of the parameters of fitting curves

predicted values of the parameters β and γ for AASC reinforced with single and multiple hooked-end steel fibres in different fibre volume fractions.

As shown in Fig. 14 and Table 5, only three different values of the parameters β and γ are used to predict the compressive stress–strain response of the AASC mixes reinforced with three different fibre types investigated in this study. Although 3D, 4D and 5D fibres differ for the number of bends at both ends of the fibre, they have the same aspect ratio (l_f/d_f), resulting in the same values of fibre reinforcing index ((l_f/d_f) • v_f) for each fibre type. Although the fibre

geometry is not taken into account, the proposed model is able to predict the compressive stress–strain response of steel fibre-reinforced AASC mixes quite accurately.

Knowing only the behaviour of the plain reference concrete under uniaxial compression and the fibre volumetric reinforcing index, the proposed model can predict the compressive response of steel fibre-reinforced composites, regardless of the matrix type and the fibre geometry and content. To verify this, the experimental stress–strain curve obtained in this study

for AASC are predicted using the proposed model and the results shown in Fig. 15.

Although the proposed model can predict quite accurately the compressive response of fibre-reinforced AASC, additional experimental data might be needed to better differentiate the model parameters for alkali-activated slag-based concrete reinforced with different steel fibres geometries.

5 Conclusions

This study investigated experimentally the compressive behaviour of alkali-activated slag-based concrete reinforced with single and multiple hooked-end steel fibres, i.e. 3D, 4D and 5D, at different volume fractions up to 0.75%. The behaviour of steel fibre-reinforced AASC was compared with the same strength grade Portland cement concrete reinforced with the same fibre types and dosages. Finally, an analytical model is proposed and calibrated using the compressive stress–strain curves obtained for PCC, steel fibre-reinforced PCC and AASC available in the literature to predict the compressive response of steel FRAASC under uniaxial compression. The proposed model does not differentiate between matrix type (i.e. PCC and AASC) and fibre geometries. The following conclusions can be drawn from this study:

- The incorporation of single and multiple hooked-end steel fibres, regardless of the fibre geometry, provides a higher compressive strength increment for AASC (with a maximum of 21.8% for AASC-5D50) than PCC (with a maximum of 1.5% for PCC-5D75).
- Single and multiple hooked-end steel fibres have a limited effect on the modulus of elasticity of both AASC and PCC, with a maximum increment of up to 3 MPa. However, the incorporation of fibres in AASC shows a higher increase in the modulus of elasticity (with a maximum of 8.7% for AASC-3D75) than PCC mixes (with a maximum of 1.2% for PCC-3D75).
- The incorporation of single and multiple hooked-end steel fibres in AASC and PCC enhances the material ductility, which can be described by the $\varepsilon_{c,max(FRC)}/\varepsilon_{c,max(REF)}$ and $\sigma_{c,u(FRC)}/\sigma_{c,u(REF)}$ ratios. In comparison to the reference mix, both AASC and PCC show an increase of strain

corresponding to the peak stress and stress at ultimate strain, resulting in softer post-peak descending branches of the compressive stress–strain curve. However, the improvement provided by the steel fibre incorporation is much more for AASC than PCC for all fibre geometries and volume fractions that were studied.

A model is proposed and calibrated on the stress-strain curves available in the literature for steel fibre-reinforced PCC and AASC in combination with the experimental data obtained in this study for PCC reinforced with 3D, 4D and 5D fibres in different volume fractions. The experimental compressive stress-strain curves obtained for AASC have been only used to validate the model, demonstrating the ability of the model to predict the stress-strain response under compression of steel fibre-reinforced AASC for different fibre content and fibre geometry. Only by knowing the compressive peak stress and corresponding strain of the concrete matrix and the fibre reinforcing index, all the model parameters can be calculated and the stress-strain curve predicted. It should be emphasised that due to the lack of available data in the literature for steel fibre-reinforced AASC, the calibration of the model proposed in this study mainly relies on the data for steel fibre-reinforced PCC. In addition, due to the lack of a significant amount of datasets on both AASC and PCC incorporating 4D and 5D steel fibres, the effect of the fibre geometry is not considered in the proposed model. With a wider amount of available datasets, this assumption may be revisited.

Declarations

Conflict of interest The authors declare that they have no known financial interests or personal relationship that could have appeared to influence the subject matter or materials discussed in this manuscript.

References

1. Ding Y, Dai J-G, Shi C-J (2016) Mechanical properties of alkali-activated concrete: a state-of-the-art review. Constr Build Mater 127:68–79. https://doi.org/10.1016/j.conbuildmat.2016.09.121

2. Provis JL, Bernal SA (2014) Geopolymers and related alkali-activated materials. Annu Rev Mater Res 44(1):299–327. https://doi.org/10.1146/annurev-matsci-070813-113515

3. Provis JL, van Deventer JSJ (eds) (2014) Alkali activated materials: state-of-the-art report, RILEM TC 224-AAM, 1st edn. Springer, Dordrecht

4. Farhan NA, Sheikh MN, Hadi MN (2019) Investigation of engineering properties of normal and high strength fly ash based geopolymer and alkali-activated slag concrete compared to ordinary Portland cement concrete. Constr Build Mater 196:26–42. https://doi.org/10.1016/j.conbuildmat.2018.11.083

5. Amer I, Kohail M, El-Feky MS, Rashad A, Khalaf MA (2021) A review on alkali-activated slag concrete. Ain Shams Eng J 12(2):1475–1499. https://doi.org/10.1016/j.asej.2020.12.003

6. El-Hassan H, Elkholy S (2021) Enhancing the performance of Alkali-Activated Slag-Fly ash blended concrete through hybrid steel fiber reinforcement. Constr Build Mater 311:125313. https://doi.org/10.1016/j.conbuildmat.2021.125313

7. Thomas RJ, Peethamparan S (2015) Alkali-activated concrete: engineering properties and stress–strain behavior. Constr Build Mater 93:49–56. https://doi.org/10.1016/j.conbuildmat.2015.04.039

8. Ding Y, Dai J-G, Shi C-J (2018) Fracture properties of alkali-activated slag and ordinary Portland cement concrete

9. Bernal SA, Mejía de Gutiérrez R, Pedraza AL, Provis JL, Rodriguez ED, Delvasto S (2011) Effect of binder content on the performance of alkali-activated slag concretes. Cem Concr Res 41(1):1–8. https://doi.org/10.1016/j.cemconres.2010.08.017

10. Chi M (2012) Effects of dosage of alkali-activated solution and curing conditions on the properties and durability of alkali-activated slag concrete. Constr Build Mater 35:240–245. https://doi.org/10.1016/j.conbuildmat.2012.04.005

11. Adesina A (2020) Performance of fibre reinforced alkali-activated composites—a review. Materialia 12:100782. https://doi.org/10.1016/j.mtla.2020.100782

12. Niş A, Eren NA, Çevik A (2021) Effects of nanosilica and steel fibers on the impact resistance of slag based self-compacting alkali-activated concrete. Ceram Int 47(17):23905–23918. https://doi.org/10.1016/j.ceramint.2021.05.099

13. Farhan NA, Sheikh MN, Hadi MNS (2018) Engineering properties of ambient cured alkali-activated fly ash-slag concrete reinforced with different types of steel fiber. J Mater Civ Eng. https://doi.org/10.1061/(ASCE)MT.1943-5533.0002333

14. Amran M, Fediuk R, Abdelgader HS, Murali G, Ozbakkaloglu T, Lee YH, Lee YY (2022) Fiber-reinforced alkali-activated concrete: a review. J Build Eng 45:103638. https://doi.org/10.1016/j.jobe.2021.103638

15. Ranjbar N, Zhang M (2020) Fiber-reinforced geopolymer composites: a review. Cem Concr Compos 107:103498. https://doi.org/10.1016/j.cemconcomp.2019.103498

16. Yuan X, Chen W, Lu Z, Chen H (2014) Shrinkage compensation of alkali-activated slag concrete and microstructural analysis. Constr Build Mater 66:422–428. https://doi.org/10.1016/j.conbuildmat.2014.05.085

17. Collins F, Sanjayan J (2001) Microcracking and strength development of alkali activated slag concrete. Cem Concr Compos 23(4–5):345–352. https://doi.org/10.1016/S0958-9465(01)00003-8

18. Bernal S, de Gutierrez R, Delvasto S, Rodriguez E (2010) Performance of an alkali-activated slag concrete reinforced with steel fibers. Constr Build Mater 24(2):208–214. https://doi.org/10.1016/j.conbuildmat.2007.10.027

19. Koenig A, Wuestemann A, Gatti F, Rossi L, Fuchs F, Fessel D, Dathe F, Dehn F, Minelli F (2019) Flexural behaviour of steel and macro-PP fibre reinforced concretes based on alkali-activated binders. Constr Build Mater 211:583–593. https://doi.org/10.1016/j.conbuildmat.2019.03.227

20. Shaikh FUA (2019) Pullout Behavior of Hook End Steel Fibers in Geopolymers. J Mater Civ Eng. https://doi.org/10.1061/(ASCE)MT.1943-5533.0002722

21. Hammad N, El-Nemr A, El-Deen Hasan H (2021) The performance of fiber GGBS based alkali-activated concrete. J Build Eng 42:102464. https://doi.org/10.1016/j.jobe.2021.102464

22. Abdallah S, Fan M, Rees DWA (2018) Bonding mechanisms and strength of steel fiber-reinforced cementitious composites: overview. J Mater Civ Eng. https://doi.org/10.1061/(ASCE)MT.1943-5533.0002154

23. Abdallah S, Rees DW, Ghaffar SH, Fan M (2018) Understanding the effects of hooked-end steel fibre geometry on the uniaxial tensile behaviour of self-compacting concrete. Constr Build Mater 178:484–494. https://doi.org/10.1016/j.conbuildmat.2018.05.191

24. Abdallah S, Fan M, Rees DW (2016) Analysis and modelling of mechanical anchorage of 4D/5D hooked end steel fibres. Mater Des 112:539–552. https://doi.org/10.1016/j.matdes.2016.09.107

25. Dehghani A, Aslani F (2021) Effect of 3D, 4D, and 5D hooked-end type and loading rate on the pull-out performance of shape memory alloy fibres embedded in cementitious composites. Constr Build Mater 273:121742. https://doi.org/10.1016/j.conbuildmat.2020.121742

26. Abdallah S, Fan M, Zhou X (2016) Effect of hooked-end steel fibres geometry on pull-out behaviour of ultra-high performance concrete. World Acad Sci Eng Technol Int J Civil Environ Eng. https://doi.org/10.5281/zenodo.1128020

27. Lee S-J, Yoo D-Y, Moon D-Y (2019) Effects of hooked-end steel fiber geometry and volume fraction on the flexural behavior of concrete pedestrian decks. Appl Sci 9(6):1241. https://doi.org/10.3390/app9061241

28. Venkateshwaran A, Tan KH, Li Y (2018) Residual flexural strengths of steel fiber reinforced concrete with multiple hooked-end fibers. Struct Concrete 19(2):352–365. https://doi.org/10.1002/suco.201700030

29. Abdallah S, Fan M, Zhou X, Le Geyt S (2016) Anchorage effects of various steel fibre architectures for concrete reinforcement. Int J Concr Struct Mater 10(3):325–335. https://doi.org/10.1007/s40069-016-0148-5

30. Chen G, Gao D, Zhu H, Song Yuan J, Xiao X, Wang W (2021) Effects of novel multiple hooked-end steel fibres on flexural tensile behaviour of notched concrete beams with various strength grades. Structures 33:3644–3654. https://doi.org/10.1016/j.istruc.2021.06.016

31. Nataraja MC, Dhang N, Gupta AP (1999) Stress–strain curves for steel-fiber reinforced concrete under compression. Cem Concr Compos 21(5–6):383–390. https://doi.org/10.1016/S0958-9465(99)00021-9

32. Oliveira Júnior LÁ de, Borges VEdS, Danin AR, Machado DVR, Araújo DdL, El Debs MK, Rodrigues PF (2010) Stress-strain curves for steel fiber-reinforced concrete in compression. Matéria (Rio J) 15(2):260–266. https://doi.org/10.1590/S1517-70762010000200025

33. Ou Y-C, Tsai M-S, Liu K-Y, Chang K-C (2012) Compressive behavior of steel-fiber-reinforced concrete with a high reinforcing index. J Mater Civ Eng 24(2):207–215. https://doi.org/10.1061/(ASCE)MT.1943-5533.0000372

34. Abbass W, Khan MI, Mourad S (2018) Evaluation of mechanical properties of steel fiber reinforced concrete with different strengths of concrete. Constr Build Mater 168:556–569. https://doi.org/10.1016/j.conbuildmat.2018.02.164

35. Ezeldin AS, Balaguru PN (1992) Normal- and high-strength fiber-reinforced concrete under compression. J Mater Civ Eng 4(4):415–429. https://doi.org/10.1061/(ASCE)0899-1561(1992)4:4(415)

36. Carreira DJ, Chu K-H (1985) Stress-strain relationship for plain concrete in compression. ACI JP 82(6):797–804. https://doi.org/10.14359/10390

37. Ruiz G, La Rosa Á de, Wolf S, Poveda E (2018) Model for the compressive stress–strain relationship of steel fiber-reinforced concrete for non-linear structural analysis. Hormigón y Acero. https://doi.org/10.1016/j.hya.2018.10.001

38. Lee S-C, Oh J-H, Cho J-Y (2015) Compressive behavior of fiber-reinforced concrete with end-hooked steel fibers. Materials 8(4):1442–1458. https://doi.org/10.3390/ma8041442

39. Hardjito D, Wallah SE, Sumajouw D, Rangan B (2005) Introducing fly ash-based geopolymer concrete: manufacture and engineering properties. In: Tam CT (ed) Proceedings of the 30th conference on our world in concrete & structures: 23–24 August 2005, Singapore, pp. 271–278. CI-Premier Pte. Ltd, Singapore

40. Collins MP, Mitchell D, MacGregor JG (1993) Structural design considerations for high-strength concrete. Concr Int 15(5):27–34

41. Noushini A, Aslani F, Castel A, Gilbert RI, Uy B, Foster S (2016) Compressive stress-strain model for low-calcium fly ash-based geopolymer and heat-cured Portland cement concrete. Cem Concr Compos 73:136–146. https://doi.org/10.1016/j.cemconcomp.2016.07.004

42. Cong X, Zhou W, Elchalakani M (2020) Experimental study on the engineering properties of alkali-activated GGBFS/FA concrete and constitutive models for performance prediction. Constr Build Mater 240:117977. https://doi.org/10.1016/j.conbuildmat.2019.117977

43. Kim S-W, Jang S-J, Kang D-H, Ahn K-L, Yun H-D (2015) Mechanical properties and eco-efficiency of steel fiber reinforced alkali-activated slag concrete. Materials 8(11):7309–7321. https://doi.org/10.3390/ma8115383

44. Ruiz G, La Rosa Á de, Poveda E, Zanon R, Schäfer M, Wolf S (2022) Compressive behavior of steel-fiber reinforced concrete in Annex L of new Eurocode 2. Hormigón y Acero. https://doi.org/10.33586/hya.2022.3092

45. Bekaert Product datasheets. https://construction.bekaert.com/en-us/construction/steel-fiber-concrete-reinforcement/dramix-solutions/toolbox/product-datasheets

46. Choi S, Thienel K-C, Shah SP (1996) Strain softening of concrete in compression under different end constraints. Mag Concr Res 48(175):103–115. https://doi.org/10.1680/macr.1996.48.175.103

47. Marar K, Erenb Ö, Yitmena İ (2011) Compression specific toughness of normal strength steel fiber reinforced concrete (NSSFRC) and high strength steel fiber reinforced concrete (HSSFRC). Mat Res 14(2):239–247. https://doi.org/10.1590/S1516-14392011005000042

48. Kotsovos MD (1983) Effect of testing techniques on the post-ultimate behaviour of concrete in compression. Mat Constr 16(1):3–12. https://doi.org/10.1007/BF02474861

49. Afroughsabet V, Biolzi L, Ozbakkaloglu T (2016) High-performance fiber-reinforced concrete: a review. J Mater Sci 51(14):6517–6551. https://doi.org/10.1007/s10853-016-9917-4

50. Farhan KZ, Johari MAM, Demirboğa R (2021) Impact of fiber reinforcements on properties of geopolymer composites: a review. J Build Eng 44:102628. https://doi.org/10.1016/j.jobe.2021.102628

51. Beglarigale A, Aydın S, Kızılırmak C (2016) Fiber-matrix bond characteristics of alkali-activated slag cement-based

composites. J Mater Civ Eng. https://doi.org/10.1061/(ASCE)MT.1943-5533.0001642

52. Suksawang N, Wtaife S, Alsabbagh A (2018) Evaluation of elastic modulus of fiber-reinforced concrete. ACI Mater J 115(2). https://doi.org/10.14359/51701920

53. Yip W-K (1996) New damage variable in failure analysis of concrete. J Mater Civ Eng 8(4):184–188. https://doi.org/10.1061/(ASCE)0899-1561(1996)8:4(184)

54. Bencardino F, Rizzuti L, Spadea G, Swamy RN (2008) Stress-strain behavior of steel fiber-reinforced concrete in compression. J Mater Civ Eng 20(3):255–263. https://doi.org/10.1061/(ASCE)0899-1561(2008)20:3(255)

55. Koniki S, Ravi Prasad D (2019) Mechanical properties and constitutive stress–strain behaviour of steel fiber reinforced concrete under uni-axial stresses. J Build Rehabil 4(1):6. https://doi.org/10.1007/s41024-019-0044-x

56. Mihai IC, Jefferson AD, Lyons P (2016) A plastic-damage constitutive model for the finite element analysis of fibre reinforced concrete. Eng Fract Mech 159:35–62. https://doi.org/10.1016/j.engfracmech.2015.12.035

57. Moradi M, Bagherieh AR, Esfahani MR (2020) Constitutive modeling of steel fiber-reinforced concrete. Int J Damage Mech 29(3):388–412. https://doi.org/10.1177/1056789519851159

58. Dhakal RP, Wang C, Mander JB (2005) Behaviour of steel fibre reinforced concrete in compression. In: Lü Z (ed) Innovation & sustainability of structures: proceedings of the international symposium on innovation & sustainability of structures in civil engineering, Southeast University Nanjing, China, November 20–22, 2005. Southeast University Press, Nanjing.

59. Shi X, Park P, Rew Y, Huang K, Sim C (2020) Constitutive behaviors of steel fiber reinforced concrete under uniaxial compression and tension. Constr Build Mater 233:117316. https://doi.org/10.1016/j.conbuildmat.2019.117316

60. Wang X, Zhang S, Wang C, Cao K, Wei P, Wang J (2019) Effect of steel fibers on the compressive and splitting-tensile behaviors of cellular concrete with millimeter-size pores. Constr Build Mater 221:60–73. https://doi.org/10.1016/j.conbuildmat.2019.06.069